

Redox-Mediated Stabilization in Zinc Molybdenum Nitrides

Elisabetta Arca,^{*,†,‡} Stephan Lany,[†] John D. Perkins,[†] Christopher Bartel,[‡] John Mangum,[§] Wenhao Sun,^{||} Aaron Holder,^{†,‡} Gerbrand Ceder,^{||,⊥} Brian Gorman,[§] Glenn Teeter,[†] William Tumas,[†] and Andriy Zakutayev^{*,†,‡}

[†]National Renewable Energy Laboratory, Golden, Colorado 80401, United States

[‡]Department of Chemical and Biological Engineering, University of Colorado Boulder, Boulder, Colorado 80309, United States

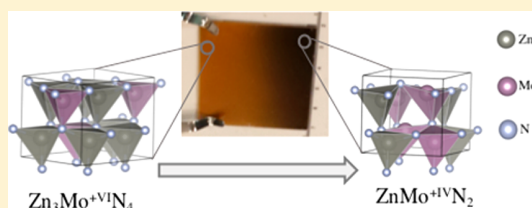
[§]Department of Metallurgical and Materials Engineering, Colorado School of Mines, Golden, Colorado 80401, United States

^{||}Materials Science Division, Lawrence Berkeley National Laboratory, Berkeley, California 94720, United States

[⊥]Department of Materials Science and Engineering, University of California Berkeley, Berkeley, California 94720, United States

Supporting Information

ABSTRACT: We report on the theoretical prediction and experimental realization of new ternary zinc molybdenum nitride compounds. We used theory to identify previously unknown ternary compounds in the Zn–Mo–N systems, Zn_3MoN_4 and $ZnMoN_2$, and to analyze their bonding environment. Experiments show that Zn–Mo–N alloys can form in broad composition range from Zn_3MoN_4 to $ZnMoN_2$ in the wurtzite-derived structure, accommodating very large off-stoichiometry. Interestingly, the measured wurtzite-derived structure of the alloys is metastable for the $ZnMoN_2$ stoichiometry, in contrast to the Zn_3MoN_4 stoichiometry, where ordered wurtzite is predicted to be the ground state. The formation of Zn_3MoN_4 – $ZnMoN_2$ alloy with wurtzite-derived crystal structure is enabled by the concomitant ability of Mo to change oxidation state from +VI in Zn_3MoN_4 to +IV in $ZnMoN_2$, and the capability of Zn to contribute to the bonding states of both compounds, an effect that we define as “redox-mediated stabilization”. The stabilization of Mo in both the +VI and +IV oxidation states is due to the intermediate electronegativity of Zn, which enables significant polar covalent bonding in both Zn_3MoN_4 and $ZnMoN_2$ compounds. The smooth change in the Mo oxidation state between Zn_3MoN_4 and $ZnMoN_2$ stoichiometries leads to a continuous change in optoelectronic properties—from resistive and semitransparent Zn_3MoN_4 to conductive and absorptive $ZnMoN_2$. The reported redox-mediated stabilization in zinc molybdenum nitrides suggests there might be many undiscovered ternary compounds with one metal having an intermediate electronegativity, enabling significant covalent bonding, and another metal capable of accommodating multiple oxidation states, enabling stoichiometric flexibility.



1. INTRODUCTION

The success of nitrides semiconductors in light-emitting devices has stimulated interest in the design and discovery of novel nitride materials for optoelectronic applications and other functionalities. The nitrides chemical space is much less explored than, for example, oxides, leaving considerable room for potential discovery of interesting new materials.¹ Experimental exploration of such broad chemical spaces is difficult and time-consuming, but it has recently been accelerated by high-throughput computations.² In addition to their potential application, nitrides are also interesting from the perspective of fundamental science: they are often metastable materials due to the inherent stability of the triple bond in the N_2 molecule and to the strength of the metal–nitrogen bonds.³

Despite the great scientific and technological interest, considerable challenges exist in synthesizing nitrides. Substantial progress has been made in designing nitride synthetic routes^{4–6} that address the difficulty of breaking the N_2 triple bond and also enable access to metastable compounds.^{1,3} These research efforts have led to discoveries of new binary

(monometallic)^{7,8} and ternary (bimetallic) nitrides. Development of computational tools, in terms of both computational power and increasing accuracy, has been pivotal to accelerating materials’ discovery in many areas.^{9,10} Nitrides are no exception to this trend, with some examples including Zn-based ternary nitrides,¹¹ as well as nitrides with layered¹² or perovskite¹³ structures. Additionally, new classes of chemical compounds have been discovered (e.g., pernitrides¹⁴), and new functionalities have been reported (e.g., ultraincompressibility¹⁵). Nitrides have been demonstrated for a variety of applications, including catalysis,¹⁶ electrocatalysis,¹⁷ dichromism,¹⁸ plasmonics,¹⁹ and thermoelectrics.²⁰

Of particular interest from both applied and basic perspectives are molybdenum-based nitrides. In solid-state chemistry, Mo-based nitrides can form covalent, ionic, or metallic compounds, depending on the Mo oxidation state. In ternary molybdenum nitrides, the latter depends on the

Received: December 5, 2017

Published: March 1, 2018

electronegativity of the second cation, M. Highly electropositive elements (electronegativity $EN \leq 1$) tend to form ionic nitridomolybdates with Mo formally in a +VI oxidation state,^{21,22} for example, M_3MoN_4 with $M = Ca, Sr, Ba$ alkaline-earth metals. The electron donation from such electropositive elements stabilizes the $[MoN_4]^{6-}$ units in monomeric, dimeric, or oligomeric forms. The less electropositive elements ($1.55 \leq EN \leq 2.22$) tend to form more covalent compounds with $MMoN_2$ stoichiometry,¹¹ where $M = Fe, Co, or Mn$, and Mo is formally in a +IV oxidation state. Transition-metal elements (Fe, Co, Ni) and Mo can also form M_3Mo_3N interstitial nitride compounds,²³ which are metallic.

In other areas of chemistry, the ability of Mo to switch between different oxidation states enables its participation in various catalytic processes, in contrast to other transition-metal elements such as Cr or W.²⁴ For example, several organisms use a Mo-containing enzyme for the N_2 fixation process.²⁵ Similarly, Mo active sites cycle from +IV to +VI oxidation states in the formate dehydrogenase (FDH) enzyme, relevant to the CO_2 reduction process.²⁶ Mo-based nitrides have also been shown to have superior performance in both oxygen reduction reactions (ORRs) and hydrogen evolution reactions (HERs), with the Mo redox flexibility being pivotal for these electrocatalytic processes.^{16,27}

Here, we report on the discovery of nitrides in the Zn–Mo–N chemical space, whose synthesis was facilitated by the ability of Mo to accommodate different oxidation states and switch between them. Despite using readily available elements, the Zn–Mo–N ternary system has not been reported in the ICDD/ICSD databases or in literature. Ab-initio calculations resulted in the prediction two new compounds with $ZnMoN_2$ and Zn_3MoN_4 stoichiometries in this chemical space. Experiments show that these two compounds and the metastable alloys at intermediate compositions form in the wurtzite-derived crystal structure. Retaining the same wurtzite-derived crystal structure across the $ZnMoN_2$ – Zn_3MoN_4 alloy composition is possible due to the ability of Mo to switch between +VI and +IV oxidation states and the stability of a covalent Zn–N framework. We also show that the optoelectronic properties of Zn–Mo–N vary dramatically as a function of composition: the Zn_3MoN_4 is resistive and has a relatively wide bandgap, whereas the $ZnMoN_2$ is a highly optically absorbing and electrically conductive material.

2. RESULTS AND DISCUSSION

2.1. Thermodynamic Stability. According to theoretical calculations, the Zn–Mo–N system should have two ternary compounds which are readily synthesizable: $ZnMoN_2$ (112-phase) with space group $P6_3mc$ (Figure 1A), and Zn_3MoN_4 (314-phase) with space group $Pmn2_1$ (Figure 1B). The main difference between these two structures is the Mo coordination (4-fold in $Pmn2_1$ and 6-fold in $P6_3mc$). Neither phase has been reported so far in the ICDD/ICSD databases or in literature. The predicted orthorhombic $Pmn2_1$ structure of the 314-phase (Figure 1B) can be described by a supercell of a wurtzite structure with ordered Zn and Mo cations in a 3:1 ratio. The orthorhombic lattice vectors are $a = 2a_{h1}$, $b = a_{h1} + 2a_{h2}$, $c = c_h$, where a_h and c_h are the hexagonal lattice vectors of the wurtzite lattice. Notably, the calculated ratio $a/b = 1.1559$ lies within 0.1% of the ideal wurtzite ratio of $2/\sqrt{3} = 1.1547$, so it would be experimentally difficult to detect such a small distortion.²⁸ In the following, we use the term “wurtzite-derived” structure to describe either the ordered or disordered arrangements of Zn

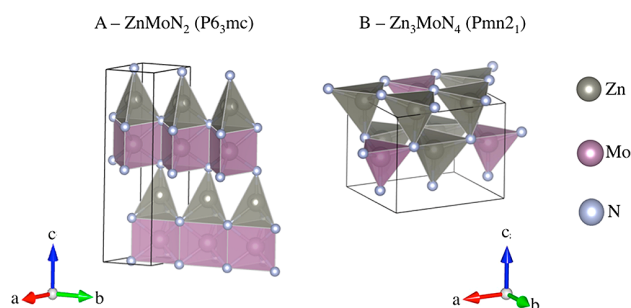


Figure 1. Predicted crystal structures of the (A) $ZnMoN_2$ with Mo in 6-fold coordination and (B) Zn_3MoN_4 compounds with Mo in 4-fold coordination. For Zn, 4-fold coordination is observed in both structures. The Mo coordination polyhedrons are magenta, and the Zn coordination polyhedrons are gray.

and Mo on the tetrahedrally coordinated cation sublattice of the underlying wurtzite structure.

The tetrahedral $[MoN_4]^{6-}$ coordination of the Mo atoms in the wurtzite-derived Zn_3MoN_4 structure ($Pmn2_1$) is similar to that in nitridomolybdates, M_3MoN_4 ($Pbca$) of alkali-earth metals ($M = Ca, Sr, Ba$)²⁹ and related materials.³⁰ The Mo–N bond in Zn_3MoN_4 is 1.87–1.89 Å, comparable to 1.87 Å in M_3MoN_4 . However, the coordination environment of the +II cation is quite different: Zn in Zn_3MoN_4 is tetrahedrally coordinated by N atoms (Figure 1B), whereas the alkali-earth atoms in nitridomolybdates are often octahedrally coordinated. The Zn–N bond length is on average ~ 2.05 Å, which is substantially shorter than the 2.60–3.05 Å Ca–N and Ba–N bond lengths observed in these orthorhombic nitridomolybdates. In contrast to the tetrahedrally (Td)-coordinated Mo(+VI) in the Zn_3MoN_4 crystal structure ($Pmn2_1$), the $ZnMoN_2$ hexagonal ($P6_3mc$) structure has Mo(+IV) in a 6-fold trigonal prismatic coordination, similar to what is observed in MoS_2 or $MnMoN_2$. The Mo–N bond length is also very similar in these compounds: 2.09–2.17 Å for the predicted $ZnMoN_2$ structure compared to 2.12 Å in $MnMoN_2$.¹¹ The Zn ions in $ZnMoN_2$ have tetrahedral coordination (Figure 1A), unlike the octahedral coordination of Mn in $MnMoN_2$. The Mo–N bonds lengths in Zn–Mo–N compounds are as expected for the different size of the Mo(+VI) and Mo(+IV): 1.87–1.89 Å in Zn_3MoN_4 and ~ 2.13 Å in $ZnMoN_2$.

To evaluate the relative stability of the Zn_3MoN_4 and $ZnMoN_2$ materials, we calculated stability regions (Figure 2A) and their polymorph energies (Figure 2B). At the $ZnMoN_2$ composition, the wurtzite-derived structure is 160 meV/atom higher in energy than the ground-state hexagonal $P6_3mc$ structure; at the Zn_3MoN_4 composition, the $P6_3mc$ ($ZnMoN_2$ -like structure) is 250 meV/atom higher in energy than the $Pmn2_1$ structure. At the intermediate Zn_2MoN_3 composition, the wurtzite-derived structure is 80 meV/atom and the $P6_3mc$ ($ZnMoN_2$ -like structure) is 260 meV/atom above the $ZnMoN_2$ – Zn_3MoN_4 convex-hull tie line (Figure 2B), so this Zn_2MoN_3 phase is higher in energy with respect to the ground-states for the two ends point (Figure 2A). As shown in Figure 2B, Zn_3MoN_4 has a wider stability region than $ZnMoN_2$ with respect to decomposition into binary competing phases, and hence, it should be easier to synthesize. Depending upon the chemical potentials of Zn and Mo, the required nitrogen chemical potential $\Delta\mu_N$ ranges from the mild conditions typical of conventional synthesis ($\Delta\mu_N$ down to -1 eV), up to highly

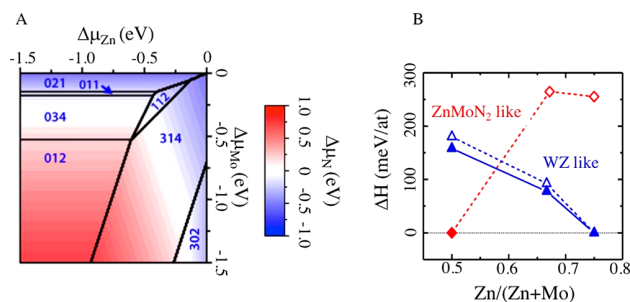


Figure 2. (A) Calculated stability diagram for the Zn–Mo–N chemical space as a function of the chemical potentials $\Delta\mu$ of Zn, Mo, and N atoms. The ijk indices denote the stable $\text{Zn}_i\text{Mo}_j\text{N}_k$ compounds. (B) Calculated enthalpies for Zn–Mo–N materials at 112, 213, and 314 compositions in two different structures, with respect to the ground-state formation enthalpies. Open symbols are random cation substitutions (five samples each), and solid symbols are cation-ordered configurations.

reactive environments achievable when a nitrogen plasma source is used ($\Delta\mu_{\text{N}}$ up to +1 eV).³¹

2.2. Crystal Structure. A representative X-ray diffraction (XRD) pattern for a Zn–Mo–N thin film with $\text{Zn}/(\text{Zn} + \text{Mo}) = 0.68$ ($f_{\text{Zn}} = 0.68$) composition deposited in 20 mTorr pressure without any intentional heating is shown in Figure 3A.

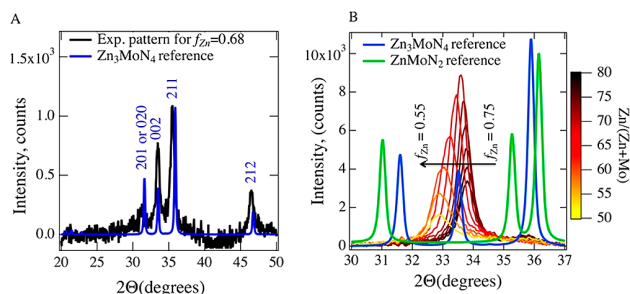


Figure 3. (A) Measured XRD pattern of the Zn–Mo–N film deposited at room temperature, compared with the simulated pattern for Zn_3MoN_4 composition. (B) XRD pattern of a Zn–Mo–N sample deposited at 200°C as a function of Zn content f_{Zn} on the relative color scale.

All the XRD peaks can be indexed to the wurtzite-derived structure, with good agreement between the simulated and measured peak positions. A slightly different peak-intensity ratio was observed for the measured XRD patterns, which is a rather common effect for thin-film samples. Additional studies employing bulk powders or single crystals, as well as more powerful diffraction sources (such as synchrotron X-ray or neutron diffraction sources), would be required for a full experimental assessment of the atoms' position.

The XRD patterns of the Zn–Mo–N films deposited at higher temperature (200 °C, 20 mTorr) or lower pressure (25 °C, 10 mTorr) have strong 002 preferential orientation, as shown for one representative case in Figure 3B. More XRD patterns as a function of cation composition (f_{Zn} from 0.95–0.35) and deposition conditions (e.g., temperature and pressure) are presented in Figure S1 of Supporting Information. The position of the 002 peak progressively shifts to lower diffraction angles as the Zn content decreases from $f_{\text{Zn}} \sim 0.76$ to $f_{\text{Zn}} \sim 0.55$ (Figures 3B and S2), although it never reaches the position typical of the 002 reflection of the

ZnMoN_2 ($P6_3mc$) structure. At this Zn-poor $f_{\text{Zn}} \sim 0.55$ composition, the crystal quality of the films degrades, as indicated by the lower intensity and higher full width at half-maximum (fwhm) of the 002 diffraction peak (Figure 3B).

The Raman spectra further corroborate the existence of the wurtzite-derived structure of the Zn_3MoN_4 material and its persistence as a function of composition (Figure 4). For the f_{Zn}

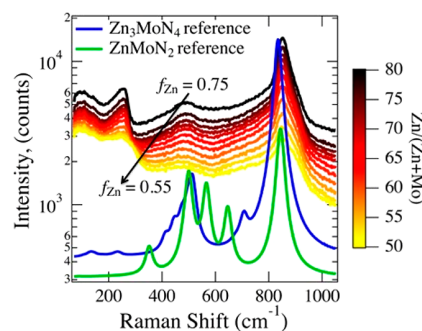


Figure 4. Comparison between the measured Raman spectra for different thin-film compositions, and the calculated Raman spectra. All the peaks present in the experimental spectra can be attributed to the simulated peaks.

= 0.75 composition, there is good agreement between the measured and calculated Raman spectra. As the composition changes between $f_{\text{Zn}} = 0.75$ and $f_{\text{Zn}} = 0.55$, the Raman spectra show a gradual change of peak intensities and a slight shift in peak positions. However, no new features appear that could be ascribed to a different structure. The Raman peaks characteristic of the wurtzite-derived structure disappear at Zn content of $f_{\text{Zn}} < 0.5$, consistent with the XRD results for the corresponding samples. For higher Mo content, the wurtzite-derived structure was not observed for the investigated synthesis conditions.

2.3. Chemical Composition. The results of the crystal structure analysis presented above suggest that Zn–Mo–N films crystallize in a wurtzite-derived structure in a broad range of X-ray fluorescence (XRF)-measured cation compositions, from $f_{\text{Zn}} = 0.8$ to $f_{\text{Zn}} = 0.5$. The N and O content of these thin films was determined by Rutherford backscattering (RBS) (see Figure S3 for raw data and fitting results). As the films get progressively Mo-rich, the nitrogen content measured by RBS decreases from $\text{Zn}_{4.4}\text{MoN}_{4.7}$ to $\text{Zn}_{0.94}\text{MoN}_{2.2}$ (Figure 5) to maintain a cation/anion ratio of ~ 1 . Assuming a charge-neutrality condition, these results would imply the lowering of the Mo oxidation state from +VI to +IV. Comparing these results to the XRD results, we determined that the most Mo-rich composition at which films are still crystalline, i.e. they display well-defined XRD peaks, is $\text{Zn}_{1.1}\text{MoN}_{2.3}$.

To rule out the possibility of any amorphous phases, which could account for a large change in stoichiometry determined by XRF and RBS on the macroscopic scale, we performed microscopic analysis on the Zn–Mo–N film having $f_{\text{Zn}} = 0.75$ and $f_{\text{Zn}} = 0.55$ compositions. The scanning transmission electron microscopy–high-angle annular dark-field (STEM-HAADF) and EDS results in Figure 6 show a homogeneous distribution of elements at the nanoscale: the modulation of the cations is only $\sim 2\%$ in amplitude and ~ 15 nm in period. These results indicate that all the elements measured by XRF and RBS are incorporated into the crystalline structure, confirming that this material is capable of accommodating large off-

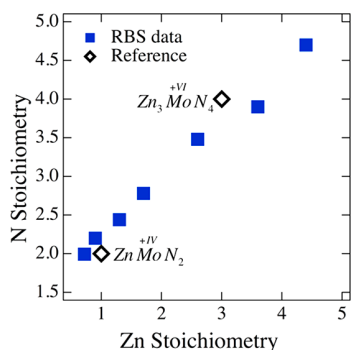


Figure 5. N stoichiometry as a function of Zn stoichiometry for Mo stoichiometry equal to 1. The N content in the films decrease as the Zn content decreases in a manner that maintains the cation/anion = 1 ratio of the wurtzite structure. This change is consistent with lowering the Mo oxidation state from +VI in Zn_3MoN_4 to +IV in $ZnMoN_2$

stoichiometry without amorphization or phase separation. We also note that oxygen is present in both films at levels higher than those determined from RBS (for $f_{Zn} = 0.75$, the oxygen content as determined by glancing angle RBS was found to be $\sim 11\%$ at. %), which is likely due to the exposure of the TEM lamellae to air while outside vacuum.

At larger scale, bright-field and dark-field TEM images of both stoichiometric and off-stoichiometric Zn–Mo–N films show columnar grain structure throughout the thickness of the film (Figure S4), as expected for samples prepared by physical vapor deposition. Also, no major impurity phases have been detected in the SAED patterns (Figures S5 and S6), consistent with the STEM-HAADF and EDS results in Figure 6. However, a very weak diffraction ring is present in a few of the raw SAED patterns, corresponding to a d -spacing of 1.16 Å. Since this ring cannot be assigned to any known binary or ternary compounds made of Zn, Mo, N, and O, we conclude that it may be attributed to an outside contamination, possibly during the

measurement. The integrated SAED patterns (Figure S5) show no sign of other diffraction peaks besides those characteristic of the Zn_3MoN_4 phase, suggesting that this outside contamination is very small.

2.4. Oxidation States. The results of composition and structure measurements indicate that crystalline Zn–Mo–N thin films retain their wurtzite-derived structure in a broad range of stoichiometries. This is possible due to the ability of Mo to assume several oxidation states, which change from +VI to +IV to maintain the charge neutrality between Zn_3MoN_4 and $ZnMoN_2$ compositions. To gain insights into the Mo oxidation state at the surfaces of Zn–Mo–N thin films, we performed X-ray photoelectron spectroscopy (XPS) measurements as a function of compositions from $f_{Zn} = 0.77$ to $f_{Zn} = 0.55$ (Figures S7 and S8). A continuous shift of all XPS peaks, i.e., Mo, N and Zn core-levels, to lower binding energies was noticed as the Zn cation fraction decreased from $f_{Zn} = 0.77$ to $f_{Zn} = 0.55$. This is consistent with a change in Fermi level position in the material as a function of composition. In addition, the shape of the Mo 3d peak changed as a function of composition.

For a more quantitative description of the Mo oxidation states, as determined at the surface, the XPS peaks were spectrally decomposed following the procedure outlined in the Supporting Information. The results are shown in Figure 7 for $f_{Zn} = 0.74$ and in Figure S8 for other compositions. For the film having $f_{Zn} = 0.74$, the main component is at 230.85 ± 0.05 eV, which is 0.85 eV higher than the value normally attributed to Mo (+IV).^{16,32} However, this value of binding energy is still lower compared to the 231.5 ± 0.2 eV that is often attributed to the formal +V oxidation state on the surface of MoO_2 or MoO_3 (Table SI in the Supporting Information).³³ In addition, a shoulder at higher binding energy (232.50 ± 0.05 eV) is present, which is usually attributed to the presence of Mo in the +VI oxidation state in oxides.

As the composition is progressively increased toward Mo-rich, another component appears at binding energy of 229.3 eV

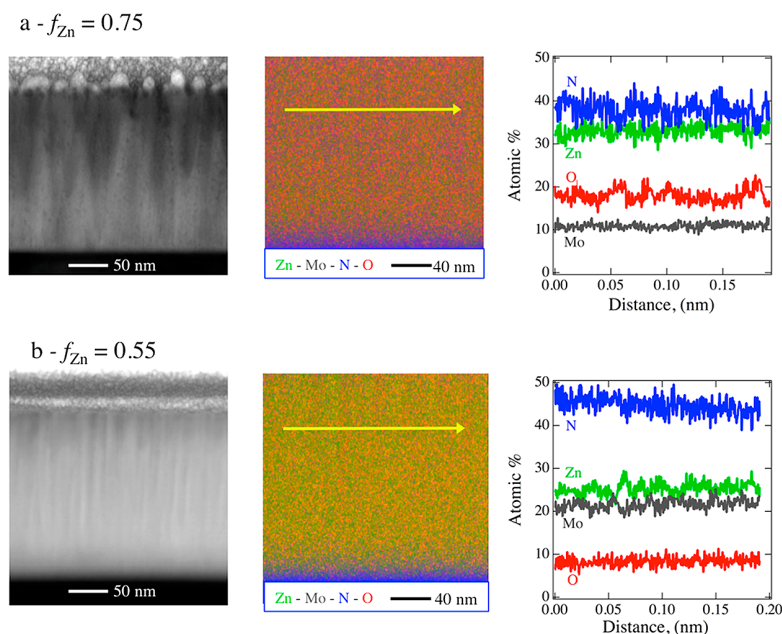


Figure 6. STEM-HAADF and EDS analysis of two Zn–Mo–N thin films having (a) $f_{Zn} = 0.75$ and (b) $f_{Zn} = 0.55$. The results show a columnar grain structure and quite homogeneous distribution of elements.

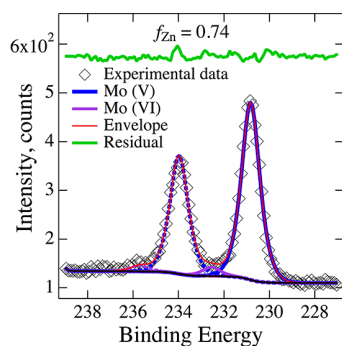


Figure 7. Deconvolution of the XPS Mo $3d_{5/2}$ and $3d_{3/2}$ peak for a Zn–Mo–N film with cation composition $f_{\text{Zn}} = 0.74$. Two principal components can be observed: violet lines attributed to +VI oxidation state and blue lines attributed to a +V oxidation state. The $3d_{5/2}$ components are shown as a solid line, and the $3d_{3/2}$ components are shown as dashed. The experimental data are shown as diamond symbols, the envelope is solid-red, the residual of the fitting is solid-green, and the background is shown in solid black.

(see Supporting Information Figure S8), a value close to that observed in molybdenum pernitride, MoN_2 (see Table SI in the Supporting Information). Nominal oxidation state in MoN_2 is +IV, however, due to the lower electronegativity and/or covalent nature of the Mo–N bond, the position of this component was attributed to a formal +3.5 oxidation state. Another interesting aspect, confirming the presence of partially filled d-states, is the appearance and steady increase of the density of states at the top of the Valence Band, corresponding to population of the Mo 4d levels, as the Mo content increases. This trend has an analogy in the $\text{MoO}_2/\text{MoO}_3$ system, where MoO_3 show no density of states in correspondence of the Mo 4d levels owing to the fact that Mo(VI) is a d^0 compounds, whereas Mo(+IV) is a d^2 , thus having populated d-levels.³³

2.5. Bonding Analysis. In order to get chemical insight into the bonding character of the calculated Zn_3MoN_4 ($Pmn2_1$) and ZnMoN_2 ($P6_3mc$) materials, we performed a Crystal Orbital Hamilton Population (COHP) and density-derived charge analysis of these compounds (Figure 8). In addition, we compared these COHP analysis results to the chemically related Sr_3MoN_4 ($Pbca$) and MnMoN_2 ($P6_3/mmc$) materials (Figure S9 in the Supporting Information) to understand the role of Zn in the stabilization of these new nitridomolybdates.

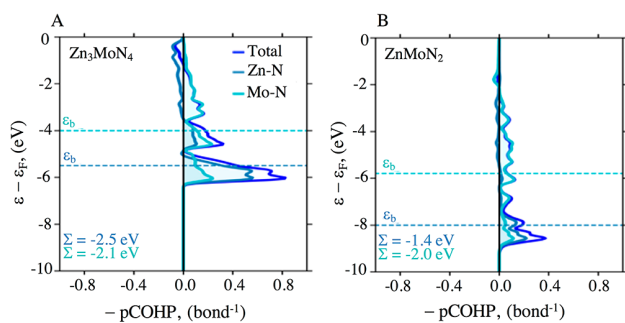


Figure 8. Crystal Orbital Hamilton Population (COHP) analysis partitioned by pairwise interactions Zn_3MoN_4 ($Pmn2_1$) and ZnMoN_2 ($P6_3mc$). In each plot, bonding and antibonding interactions appear on the right and left side of the vertical black line, respectively. ϵ_b is the center (first moment) of the total bonding distribution, and Σ is the net bond energy (see the Supporting Information for details).

As shown in Figure 8, the bonding states are qualitatively similar between the Zn_3MoN_4 in $Pmn2_1$ structure and ZnMoN_2 in $P6_3mc$ structure, with substantial bonding present for both Mo–N and Zn–N at similar energies. While the covalent bonding is deeper for both Zn–N and Mo–N in ZnMoN_2 compared with Zn_3MoN_4 , the extent of the covalent bonding (net bonding area (Σ)) is greater in Zn_3MoN_4 , primarily due to increased covalency of Zn–N interactions. The layered tetrahedra $[\text{ZnN}_4]/[\text{MoN}_4]$ of Zn_3MoN_4 thus enable increased overall covalency for Zn–N and increased chemical hardness compared with the alternating $[\text{ZnN}_4]$ tetrahedra and $[\text{MoN}_6]$ octahedra of the ZnMoN_2 arrangement. Zn_3MoN_4 also exhibits increased charge transfer between cations and nitrogen anions compared with the metallic ZnMoN_2 , which we quantify by analyzing the ratio of summed bond-orders to density derived electrostatic charges. This is to be expected as the density-derived charge increases by ~ 1 eV for Mo in Zn_3MoN_4 compared with ZnMoN_2 , aligning with the increase in oxidation state from +IV to +VI (Figure S8). The favorable mixed covalency bonding arrangement of the Zn_3MoN_4 structure leads to a significant bandgap (compared with the electrically conductive ZnMoN_2) and retention of the wurtzite-derived structure even as f_{Zn} is decreased.

The structural transition from $Pmn2_1$ to $P6_3mc$ would require significant rearrangement: from $[\text{ZnN}_4]$ and $[\text{MoN}_4]$ tetrahedra in Zn_3MoN_4 ($Pmn2_1$), to layered $[\text{ZnN}_4]$ tetrahedra and $[\text{MoN}_6]$ octahedra in ZnMoN_2 ($P6_3mc$). Thus, as f_{Zn} is decreased from 0.75 to 0.50 and the thermodynamic driving force for forming Mo octahedra is increasing, the metastable wurtzite-derived structure remains favorable for Zn bonding and is kinetically preserved due to the reconstructive barrier toward forming the ordered layers of the 112 structure.

2.6. Optoelectronic Properties. The influence of the changing Mo oxidation state on the optoelectronic properties of the Zn–Mo–N material is dramatic. As shown in Figure 9A,

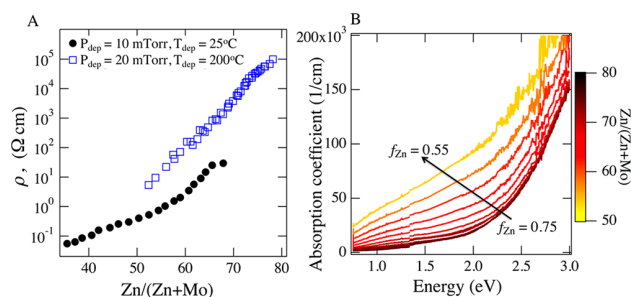


Figure 9. (A) Effect of the chemical composition on the electrical properties of the Zn_3MoN_4 – ZnMoN_2 films. As the Mo concentration increases, the resistivity decreases. (B) Absorption coefficient as a function of cation composition from Zn_3MoN_4 to ZnMoN_2 . Increasing the Mo content considerably enhances the absorbance of the thin films.

stoichiometric Zn_3MoN_4 samples are quite resistive (10^4 – $10^5 \Omega\text{cm}$). The resistivity decreases with decreasing f_{Zn} down to 10^{-1} – $10^0 \Omega\text{cm}$ at the ZnMoN_2 composition. Thus, the resistivity of the films varies over 5 orders of magnitude for compositions where the material is crystalline and isostructural. This is remarkable because doping control in nitrides is usually quite challenging and requires careful tuning of processing conditions. A small dependence of resistivity on the deposition conditions was noticed, as well. For the samples having the

same cation composition in the $f_{\text{Zn}} = 0.5\text{--}0.7$ range, $10\times$ lower resistivity is achieved when the films are grown at $25\text{ }^\circ\text{C}$ and 10 mTorr , compared to $200\text{ }^\circ\text{C}$ and 20 mTorr . It is also interesting to note that ZnMoN_2 films display temperature-activated conductivity in the $150\text{--}350\text{ K}$ region (Figure S10A), unlike the previously known metallic ternary molybdenum nitrides. Hall measurements were attempted on the ZnMoN_2 thin films but were not successful, which implies that the carrier mobility is less than $0.1\text{ cm}^2\text{ V}^{-1}\text{ s}^{-1}$ for these polycrystalline samples.

Optical properties of Zn–Mo–N also change as a function of composition. Progressive enrichment in Mo and the change of its oxidation state led to an increase in the absorption coefficient (Figure 9B) and a substantial reduction of the transmittance of the films (Figure S10B). The optical bandgap, estimated from the kink in the slope of the squared value of the optical absorption spectrum, is in the order of 2.4 eV for $f_{\text{Zn}} = 0.75$ (Figure S11). Also, the overall absorption coefficient increases as a function of increasing Mo content. The resulting pale-yellow coloration for the Zn_3MoN_4 thin films coincides with the yellow color of the single crystals of both Sr_3MoN_4 and Ba_3MoN_4 nitromolybdates reported in literature. In comparison with the 2.4 eV optical bandgap of Zn_3MoN_4 thin films, the GW-calculated indirect and direct bandgaps for the Zn_3MoN_4 in cation-ordered orthorhombic structure are 3.82 and 3.98 eV , respectively. The difference between the experimental optical absorption onset and the theoretical band gap determined by GW calculations, could be due to Zn/Mo cation disorder and/or oxygen contamination in experimental samples. Atomic disorder has been widely studied in several materials systems and shown to play an active role in affecting the band gap of the material, and thus its optical properties.^{28,34–37} Preliminary results on the Zn_3MoN_4 material show that disorder can induce a substantial reduction of the band gap, to values comparable to the experimental results.

3. DISCUSSION

Two new compounds with Zn_3MoN_4 and ZnMoN_2 stoichiometries have been synthesized and characterized, following the theoretical predictions. The calculations suggest that new ternary nitrides are likely to be observed in the Zn–Mo–N ternary system (Figure 1) and predict thermodynamic stability regions of these Zn_3MoN_4 ($Pmn2_1$) and ZnMoN_2 ($P6_3mc$) compounds (Figure 2). Structural measurements indicate that both nitrides crystallize in the wurtzite-derived structure in the $0.75 < f_{\text{Zn}} \leq 0.50$ composition range (Figures 3 and 4). As the material becomes Mo-rich, the measured anion/cation ratio remains constant (Figures 5 and 6) and the Mo oxidation state varies (Figures 5 and 7). The theoretical COHP analysis results (Figure 8) corroborate these experimental observations, and also suggest significant Zn–N bonding in both Zn_3MoN_4 ($Pmn2_1$) and ZnMoN_2 ($P6_3mc$) compounds, in contrast to Sr_3MoN_4 ($Pbca$) which is predominantly stabilized by Mo–N bonding. The optical absorption coefficient at 2 eV increases by $10\times$, and the electrical conductivity increases by 10^5 , going from Zn_3MoN_4 to ZnMoN_2 end-member points of the alloy (Figure 9).

Experimental XRD results (Figures 3 and 4) indicate the formation of a $\text{ZnMoN}_2\text{--Zn}_3\text{MoN}_4$ alloy with wurtzite-derived structure. On the other hand, according to theoretical calculations, the wurtzite-derived structure at ZnMoN_2 composition is 160 meV/atom higher in energy compared to the hexagonal $P6_3mc$ structure (Figure 2). However, even higher mixing enthalpies ($\sim 400\text{ meV/atom}$) have recently been

observed in $(\text{Sn,Ti})_3\text{N}_4$,³⁸ typical for metastable heterostructural alloys.³⁹ Additionally, in the wurtzite-derived structure, DFT calculations predict a contraction of the ZnMoN_2 lattice parameters compared to Zn_3MoN_4 lattice parameters. In contrast, the closest agreement with the measured XRD and selected-area electron diffraction (SAED) patterns is achieved for a simulated wurtzite-derived structure with lattice parameters expanded by 1.5% . Thus, further theoretical studies making use of cluster expansion or Monte Carlo methods would be required to assess if lower-energy configurations of wurtzite-derived structures exist at ZnMoN_2 composition.

The RBS composition analysis (Figure 6), combined with the XPS results (Figure 7), suggest a rather complex situation for the Mo oxidation state in Zn–Mo–N thin films. The bulk RBS analysis implies that the Mo oxidation state shifts from nominally +VI to +IV as the stoichiometry changes from Zn_3MoN_4 to ZnMoN_2 , based on formal charge count with Zn in +II oxidation state and N in -III oxidation state. From more surface-sensitive XPS analysis, it appears that some Mo peak components have binding energies characteristic of the +VI and +V oxidation state for the stoichiometric Zn_3MoN_4 phase and an increasing concentration of +3.5 for the more Mo-rich compositions. For this Mo-rich composition, alongside the Mo +3.5 components, at least two other components are present, which could be attributed to the +V and +VI oxidation state. The presence of multiple oxidation states suggests that the nature of the Mo–N bond in Zn_3MoN_4 is not completely ionic. This is also supported by the presence of significant covalent bonding states for Mo–N (Figure 8).

There are several likely reasons for the formation of the metastable alloys with wurtzite structure in the composition range from Zn_3MoN_4 to ZnMoN_2 . First, according to the combination of RBS and XPS measurements, the ability of Mo to adopt different oxidation states from +VI to +IV helps to accommodate a range of Zn/Mo stoichiometries. Second, this range can be accommodated by the ability of Zn to contribute to the bonding states of both Zn_3MoN_4 and ZnMoN_2 materials, as shown by the COHP analysis (Figure 8). The wide stoichiometry range in Zn–Mo–N materials is different than the fixed M_3MoN_4 stoichiometry of the previously reported nitridomolybdates based on highly electropositive $\text{M} = \text{Ca, Sr, and Ba}$ elements. Thus, it appears that the propensity for Zn to contribute to the bonding states, coupled with the ability of Mo to stabilize both +VI and +IV oxidation states, together enable the formation of Zn–Mo–N alloys with a wide range of stoichiometry.

Based on the results and discussion presented above, we propose the concept of “redox-mediated stabilization” to describe the formation of Zn–Mo–N materials with wurtzite-derived structure in a broad range of chemical compositions, enabled by change in the oxidation state of Mo. This concept is expected to extend beyond the Zn–Mo–N family and be applicable to other solid-state materials. In pnictides, other possible materials classes that could show redox-mediated stabilization include II–IV–Pn_2 , $\text{II}_2\text{–V–Pn}_3$, and $\text{II}_3\text{–VI–Pn}_4$ compounds, where II is a relatively electropositive element that contributes to the bonding states; IV, V, and VI are transition metals that can access higher or lower oxidation states; and Pn is an element belonging to the pnictides family (e.g., N, P, As). One past example of chalcogenide materials showing a similar redox-mediated stabilization in the $\text{Cu}_2\text{SnS}_3\text{–Cu}_3\text{SnS}_4$ system,⁴⁰ where the stoichiometry variation is accommodated by the change in Cu from I+ to II+ oxidation states without

altering the zincblende-derived crystal structure. A few examples in oxides that we are aware of include Cr_2MnO_4 – CrMn_2O_4 ⁴¹ and Fe_2MnO_4 – FeMn_2O_4 , both with spinel-derived crystal structures.

4. CONCLUSIONS

Redox-mediated stabilization of the crystal structure has been demonstrated in the newly discovered Zn–Mo–N ternary material system. Experimentally, we have shown that it is possible to tune the stoichiometry from Zn_3MoN_4 to ZnMoN_2 while retaining the wurtzite-derived crystal structure. Theoretical calculations suggest that the cation-ordered wurtzite with $Pmn2_1$ symmetry has the lowest energy only for the Zn_3MoN_4 composition, whereas the ZnMoN_2 composition should crystallize in the hexagonal structure with $P6_3mc$ symmetry. The results of the combined theoretical and experimental analysis suggest that the formation of the metastable wurtzite Zn_3MoN_4 – ZnMoN_2 alloy is possible because (1) Mo can accommodate multiple oxidation states, from +IV to +VI, allowing this smooth transition; and (2) Zn has an intermediate electronegativity and contributes to the bonding character of both Zn_3MoN_4 and ZnMoN_2 phases. The impact of the tunable composition on the optoelectronic properties is dramatic: Zn_3MoN_4 is a semitransparent and relatively resistive, whereas ZnMoN_2 is an electrically conductive and optically absorbing material. The demonstration of redox-mediated stabilization in the Zn–Mo–N system opens up the possibility to tune the properties by the concurrent change in chemical composition and oxidation state in many other materials with wurtzite and other crystal structures. Additional theoretical and synthetic efforts are currently underway to show the redox-mediated stabilization in other material systems.

5. METHODS

5.1. Experimental Methods. Experimental synthesis of Zn–Mo–N thin-film sample libraries was performed using combinatorial cosputtering of Mo and Zn metals in the presence of N plasma on glass substrates in a deposition chamber with $<1 \times 10^{-6}$ Torr base pressure. Two sputtering guns were loaded with 2"-diameter Mo and Zn metal targets and positioned at 45° with respect to the substrate normal to achieve a cation compositional gradient; the N plasma source was aligned to the normal.⁴² To access a broad range of Zn/Mo ratios, we used gun powers in the range of 25–45 W. Before the deposition, the 2" × 2" Eagle-XG glass substrates were cleaned by degreasing in water and soap, followed by ultrasonic cleaning in acetone and isopropanol baths. Depositions were performed at ambient substrate temperature to maximize the N-chemical potential, or on the heated substrate (200 °C) to improve the crystallinity. The flow of the gases was set to 10 and 30 sccm for Ar and N₂, respectively. The sputtering pressure was adjusted between 20 and 10 mTorr, to change from more nitridizing to more reducing conditions during the growth. Using this combinatorial synthesis approach, it took three sample libraries to cover the entire region of interest for cation compositions.

Spatially resolved characterization of the thin-film sample libraries was performed on a 4 × 11 grid of samples, 4 rows and 11 columns, with the compositional gradient along the 11 positions in one row.⁴³ The composition was determined by quantitative XRF on a Fischer Scientific (Fischerscope XDV-SDD) instrument using a spot size of 3 mm in diameter. The structure was characterized using a Bruker D8 XRD in Cu K α radiation, equipped with a two-dimensional (2-D) detector and a spot size on the order of 2 mm × 3 mm. Raman mapping was performed on a Reinshaw system, using a Nd:YAG laser source (532 nm). The optical transmittance and reflectance were measured in the wavelength range of 300–1700 nm on a home-built ultraviolet–visible light–near-infrared (UV–vis–NIR) spectrometer

(no integrating sphere) with a spot diameter of ~1 mm. Electrical conductivity was measured using a custom four-point probe measurement instrument with tungsten probe spacing of 1 mm. The analysis of the characterization results was performed using custom-written procedures in the Wavemetrics IGOR Pro software package. The resulting data are available at hitem.nrel.gov.

For a few selected locations on each sample library, additional detailed characterization experiments were performed. X-ray photoelectron spectroscopy measurements were performed on a Kratos Axis Nova instrument with Al K α X-ray source. The effects of surface oxidation on the measurement results were minimized by analyzing samples on the same library and by quickly transferring the samples between deposition and characterization chambers. Rutherford backscattering was performed using a model 35-MR10 RBS system from National Electrostatics Corporation, with either high (168°, RBS) or low (110°, RBG) scattering angles. Microscopy was performed on an FEI Co. Talos F200X instrument in transmission electron microscopy, selected-area electron diffractions, and energy-dispersive spectroscopy modes, on specimens prepared using the focused ion beam (FIB) lift-out method. More RBS and TEM characterization details are provided in [Supporting Information](#).

5.2. Computational Methods. The initial computational search for novel ternary metal nitrides was performed by starting from the known ternary nitrides and applying rational chemical substitutions to them, so as to extend the sampling to previously unreported compounds (DMSP algorithm).⁴⁴ The stability of these new candidate crystal structures was evaluated by comparing their density functional theory (DFT) formation energies to those of all potential competing phases. Such a search was performed in 942 ternary metal-nitride chemical spaces (M₁-M₂-N) leading to hundreds of novel compounds found to be stable. In the previously unexplored Zn–Mo–N space Zn_2MoN_3 was identified to be stable (negative formation energy).

To sample more comprehensively the Zn–Mo–N ternary space for possible compositions and their structures, we used a modified version of the Kinetically Limited Minimization (KLM) algorithm, originally designed to sample amorphous structures,⁴⁵ so to obtain a wider range of possible stoichiometries and their structures. This search was performed for many $\text{Zn}_i\text{Mo}_j\text{N}_k$ stoichiometries ($ijk = 112, 146, 414, 213, 124, 326, 338, 313$) chosen to accommodate the Zn^{2+} , $\text{Mo}^{4+/5+/6+}$, and N^{3-} oxidation states. However, only the ZnMoN_2 and Zn_3MoN_4 compositions were found to be stable against the binary competing phases. As the competing phases, we considered known materials Zn_3N_2 (space group SG 206), Mo_2N (SG 11), MoN (SG 186), as well as KLM-predicted materials Mo_3N_4 (SG 9), and a recently reported MoN_2 (SG160) pernitride.⁴⁶ The symmetry analysis for all structures was performed with the FINDSYM software.⁴⁷ The Crystallographic Information Files (CIF) were loaded into the MAUD program to simulate the reference XRD pattern. More details of the KLM calculations and the CIF files for all new stable structures are provided as [Supporting Information](#).

The first-principles calculations in DFT and in the GW approximation were performed with the VASP code,⁴⁸ using the PBE+U functional⁴⁹ with $U = 3$ eV for Mo-d.⁵⁰ Final total energies were calculated with an energy cutoff of 520 eV and a number of approximately $4000/n_{\text{at}}$ k-points in the full Brillouin zone, where n_{at} is the number of atoms in the unit cell. To calculate accurate lattice parameters, we performed van der Waals-corrected DFT calculations employing the optB86b-vdW functional.⁵¹ Within the KLM search, we successively increased the convergence criteria for samples that are likely to be accepted in the KLM sequence, while more quickly discarding unlikely high-energy structures. For evaluating the formation enthalpies and thermodynamic stability ranges of the charge-balanced compounds, we used the fitted elemental reference energies μ_{FERE} .⁵² For noncharge-balanced materials such as Mo_2N , we use a weighted average between μ_{FERE} (Mo) and the DFT energy of metallic Mo. All electronic structure calculations reported here rely on band gap corrected many body perturbation theory (GW approximation) and do not depend significantly of computational parameters like U . Crystal Orbital Hamilton Population (COHP) analysis was performed with the LOBSTER code⁵³ whereas density-derived charges

were obtained using the DDEC methods (see the [Supporting Information](#) for more details).

■ ASSOCIATED CONTENT

■ Supporting Information

The Supporting Information is available free of charge on the ACS Publications website at DOI: [10.1021/jacs.7b12861](https://doi.org/10.1021/jacs.7b12861).

X-ray diffraction, Rutherford backscattering, electron microscopy, photoemission spectroscopy, bonding analyses, optoelectronic properties, experimental methods, and computational methods (PDF)

Zn₃MoN₄ structure (CIF)

ZnMoN₂ structure (CIF)

■ AUTHOR INFORMATION

Corresponding Authors

*Elisabetta.Arca@nrel.gov

*Andriy.Zakutayev@nrel.gov

ORCID

Elisabetta Arca: [0000-0003-0651-6000](https://orcid.org/0000-0003-0651-6000)

Andriy Zakutayev: [0000-0002-3054-5525](https://orcid.org/0000-0002-3054-5525)

Notes

The authors declare no competing financial interest.

■ ACKNOWLEDGMENTS

This work was supported by the U.S. Department of Energy under Contract No. DE-AC36-08GO28308 with Alliance for Sustainable Energy, LLC, the Manager and Operator of the National Renewable Energy Laboratory. Funding provided by Office of Science, Office of Basic Energy Sciences, as part of the Energy Frontier Research Center “Center for Next Generation of Materials Design: Incorporating Metastability”.

■ REFERENCES

- (1) Zakutayev, A. J. *Mater. Chem. A* **2016**, *4*, 6742.
- (2) Curtarolo, S.; Hart, G. L. W.; Nardelli, M. B.; Mingo, N.; Sanvito, S.; Levy, O. *Nat. Mater.* **2013**, *12*, 191.
- (3) Sun, W.; Dacek, S. T.; Ong, S. P.; Hautier, G.; Jain, A.; Richards, W. D.; Gamst, A. C.; Persson, K. A.; Ceder, G. *Sci. Adv.* **2016**, *2*, e1600225.
- (4) Luo, H.; Wang, H.; Zou, G.; Bauer, E.; McCleskey, T. M.; Burrell, A. K.; Jia, Q. *Trans. Electr. Electron. Mater.* **2010**, *11*, 54.
- (5) Parkin, I. P.; Rowley, A. T. *J. Mater. Chem.* **1995**, *5*, 909.
- (6) Horvath-Bordon, E.; Riedel, R.; Zerr, A.; McMillan, P. F.; Auffermann, G.; Prots, Y.; Bronger, W.; Knierp, R.; Kroll, P. *Chem. Soc. Rev.* **2006**, *35*, 987.
- (7) Caskey, C. M.; Holder, A.; Shulda, S.; Christensen, S. T.; Diercks, D.; Schwartz, C. P.; Biagioni, D.; Nordlund, D.; Kukliansky, A.; Natan, A.; Prendergast, D.; Orvananos, B.; Sun, W.; Zhang, X.; Ceder, G.; Ginley, D. S.; Tumas, W.; Perkins, J. D.; Stevanovic, V.; Pylypenko, S.; Lany, S.; Richards, R. M.; Zakutayev, A. J. *Chem. Phys.* **2016**, *144*, 144201.
- (8) Sun, W.; Holder, A.; Orvananos, B.; Arca, E.; Zakutayev, A.; Lany, S.; Ceder, G. *Chem. Mater.* **2017**, *29*, 6936.
- (9) Savory, C. N.; Ganose, A. M.; Scanlon, D. O. *Chem. Mater.* **2017**, *29*, 5156.
- (10) Hautier, G.; Jain, A.; Ong, S. P. *J. Mater. Sci.* **2012**, *47*, 7317.
- (11) Hinuma, Y.; Hatakeyama, T.; Kumagai, Y.; Burton, L. A.; Sato, H.; Muraba, Y.; Iimura, S.; Hiramatsu, H.; Tanaka, I.; Hosono, H.; Oba, F. *Nat. Commun.* **2016**, *7*, 11962.
- (12) Bem, D. S.; Lampe-Önnerud, C. M.; Olsen, H. P.; zur Loye, H.-C. *Inorg. Chem.* **1996**, *35*, 581.
- (13) Sarmiento-Pérez, R.; Cerqueira, T. F. T.; Körbel, S.; Botti, S.; Marques, M. A. L. *Chem. Mater.* **2015**, *27*, 5957.
- (14) Gregoryanz, E.; Sanloup, C.; Somayazulu, M.; Badro, J.; Fiquet, G.; Mao, H.-k.; Hemley, R. J. *Nat. Mater.* **2004**, *3*, 294.
- (15) Bhadram, V. S.; Kim, D. Y.; Strobel, T. A. *Chem. Mater.* **2016**, *28*, 1616.
- (16) Perret, N.; Alexander, A.-M.; Hunter, S. M.; Chung, P.; Hargreaves, J. S. J.; Howe, R. F.; Keane, M. A. *Appl. Catal., A* **2014**, *488*, 128.
- (17) Cao, B.; Veith, G. M.; Neuefeind, J. C.; Adzic, R. R.; Khalifah, P. G. *J. Am. Chem. Soc.* **2013**, *135*, 19186.
- (18) Dickman, M. J.; Lattner, S. E. *J. Am. Chem. Soc.* **2016**, *138*, 10636.
- (19) Metaxa, C.; Kassavetis, S.; Pierson, J. F.; Gall, D.; Patsalas, P. *ACS Appl. Mater. Interfaces* **2017**, *9*, 10825.
- (20) Ohkubo, I.; Mori, T. *Chem. Mater.* **2014**, *26*, 2532.
- (21) Niewa, R.; Jacobs, H. *Chem. Rev.* **1996**, *96*, 2053.
- (22) Höhn, P.; Knierp, R. *Z. Kristallogr. - New Cryst. Struct.* **2000**, *215*, 325.
- (23) Alconchel, S.; Sapiña, F.; Beltrán, D.; Beltrán, A. J. *Mater. Chem.* **1998**, *8*, 1901.
- (24) Burgmayer, S. J. N.; Stiefel, E. I. *J. Chem. Educ.* **1985**, *62*, 943.
- (25) Brown, K. A.; Harris, D. F.; Wilker, M. B.; Rasmussen, A.; Khadka, N.; Hamby, H.; Keable, S.; Dukovic, G.; Peters, J. W.; Seefeldt, L. C.; King, P. W. *Science* **2016**, *352*, 448.
- (26) Robinson, W. E.; Bassegoda, A.; Reisner, E.; Hirst, J. J. *Am. Chem. Soc.* **2017**, *139*, 9927.
- (27) Zhang, Y.; Ouyang, B.; Xu, J.; Chen, S.; Rawat, R. S.; Fan, H. J. *Adv. Energy Mater.* **2016**, *6*, 1600221.
- (28) Lany, S.; Fioretti, A. N.; Zawadzki, P. P.; Schelhas, L. T.; Toberer, E. S.; Zakutayev, A.; Tamboli, A. C. *Phys. Rev. Materials* **2017**, *1*, 035401.
- (29) Baker, C. F.; Barker, M. G.; Blake, A. J.; Wilson, C.; Gregory, D. H. *Dalton Trans* **2003**, *0*, 1065.
- (30) Bailey, M. S.; McGuire, M. A.; DiSalvo, F. J. *Z. Anorg. Allg. Chem.* **2004**, *630*, 2177.
- (31) Caskey, C. M.; Richards, R. M.; Ginley, D. S.; Zakutayev, A. *Mater. Horiz.* **2014**, *1*, 424.
- (32) Xiao, X.; Yu, H.; Jin, H.; Wu, M.; Fang, Y.; Sun, J.; Hu, Z.; Li, T.; Wu, J.; Huang, L.; Gogotsi, Y.; Zhou, J. *ACS Nano* **2017**, *11*, 2180.
- (33) Scanlon, D. O.; Watson, G. W.; Payne, D. J.; Atkinson, G. R.; Egdel, R. G.; Law, D. S. L. *J. Phys. Chem. C* **2010**, *114*, 4636.
- (34) Scanlon, D. O.; Walsh, A. *Appl. Phys. Lett.* **2012**, *100*, 251911.
- (35) Martinez, A. D.; Fioretti, A. N.; Toberer, E. S.; Tamboli, A. C. *J. Mater. Chem. A* **2017**, *5*, 11418.
- (36) Veal, T. D.; Feldberg, N.; Quackenbush, N. F.; Linhart, W. M.; Scanlon, D. O.; Piper, L. F. J.; Durbin, S. M. *Adv. Energy Mater.* **2015**, *5*, 1501462.
- (37) Quayle, P. C.; Blanton, E. W.; Punya, A.; Junno, G. T.; He, K.; Han, L.; Zhao, H.; Shan, J.; Lambrecht, W. R. L.; Kash, K. *Phys. Rev. B: Condens. Matter Mater. Phys.* **2015**, *91*, 205207.
- (38) Bikowski, A.; Siol, S.; Gu, J.; Holder, A.; Mangum, J. S.; Gorman, B.; Tumas, W.; Lany, S.; Zakutayev, A. *Chem. Mater.* **2017**, *29*, 6511.
- (39) Holder, A. M.; Siol, S.; Ndione, P. F.; Peng, H.; Deml, A. M.; Matthews, B. E.; Schelhas, L. T.; Toney, M. F.; Gordon, R. G.; Tumas, W.; Perkins, J. D.; Ginley, D. S.; Gorman, B. P.; Tate, J.; Zakutayev, A.; Lany, S. *Sci. Adv.* **2017**, *3*, e1700270.
- (40) Baranowski, L. L.; Zawadzki, P.; Christensen, S.; Nordlund, D.; Lany, S.; Tamboli, A. C.; Gedvilas, L.; Ginley, D. S.; Tumas, W.; Toberer, E. S.; Zakutayev, A. *Chem. Mater.* **2014**, *26*, 4951.
- (41) Peng, H.; Zakutayev, A.; Lany, S.; Paudel, T. R.; d’Avezac, M.; Ndione, P. F.; Perkins, J. D.; Ginley, D. S.; Nagaraja, A. R.; Perry, N. H.; Mason, T. O.; Zunger, A. *Adv. Funct. Mater.* **2013**, *23*, 5267.
- (42) Fioretti, A. N.; Zakutayev, A.; Moutinho, H.; Melamed, C.; Perkins, J. D.; Norman, A. G.; Al-Jassim, M.; Toberer, E. S.; Tamboli, A. C. *J. Mater. Chem. C* **2015**, *3*, 11017.
- (43) Zakutayev, A.; Luciano, F. J., IV; Bollinger, V. P.; Sigdel, A. K.; Ndione, P. F.; Perkins, J. D.; Berry, J. J.; Parilla, P. A.; Ginley, D. S. *Rev. Sci. Instrum.* **2013**, *84*, 053905.

- (44) Hautier, G.; Fischer, C. C.; Jain, A.; Mueller, T.; Ceder, G. *Chem. Mater.* **2010**, *22*, 3762.
- (45) Zawadzki, P. P.; Perkins, J.; Lany, S. *Phys. Rev. B: Condens. Matter Mater. Phys.* **2014**, *90*, 094203.
- (46) Yu, S.; Huang, B.; Jia, X.; Zeng, Q.; Oganov, A. R.; Zhang, L.; Frapper, G. J. *Phys. Chem. C* **2016**, *120*, 11060.
- (47) Stokes, H. T.; Hatch, D. M. *J. Appl. Crystallogr.* **2005**, *38*, 237.
- (48) Shishkin, M.; Kresse, G. *Phys. Rev. B: Condens. Matter Mater. Phys.* **2006**, *74*, 035101.
- (49) Dudarev, S. L.; Botton, G. A.; Savrasov, S. Y.; Humphreys, C. J.; Sutton, A. P. *Phys. Rev. B: Condens. Matter Mater. Phys.* **1998**, *57*, 1505.
- (50) Lany, S. *Phys. Rev. B: Condens. Matter Mater. Phys.* **2013**, *87*, 085112.
- (51) Klimeš, J.; Bowler, D. R.; Michaelides, A. *Phys. Rev. B: Condens. Matter Mater. Phys.* **2011**, *83*, 195131.
- (52) Stevanović, V.; Lany, S.; Zhang, X.; Zunger, A. *Phys. Rev. B: Condens. Matter Mater. Phys.* **2012**, *85*, 115104.
- (53) Maintz, S.; Deringer, V. L.; Tchougréeff, A. L.; Dronskowski, R. *J. Comput. Chem.* **2016**, *37*, 1030.